ACS APPLIED MATERIALS & INTERFACES

Research Article

Cite This: ACS Appl. Mater. Interfaces 2017, 9, 44550−44559

www.acsami.org

$MoSe_2$ Nanosheet Array with Layered MoS_2 Heterostructures for Superior Hydrogen Evolution and Lithium Storage Performance

Jing Yang,[†] Jixin Zhu,[‡] Jingsan Xu,[§] Chao Zhang,*[,†] and Tianxi Liu*[,†]

[†]State Key Laboratory for Modification of Chemical Fibers and Polymer Materials, College of Materials Science and Engineering, Donghua University, Shanghai 201620, P. R. China

[‡]Key Laboratory of Flexible Electronics (KLOFE) & Institute of Advanced Materials (IAM), Jiangsu National Synergetic Innovation Center for Advanced Materials (SICAM), Nanjing Tech University (Nanjing Tech), 30 South Puzu Road, Nanjing 211816, P. R. China

[§]School of Chemistry, Physics and Mechanical Engineering, Queensland University of Technology, Brisbane, QLD 4001, Australia

Supporting Information

ABSTRACT: Engineering heterostructures of transition metal disulfides through low-cost and high-yield methods instead of using conventional deposition techniques still have great challenges. Herein, we present a conveniently operated and low-energy-consumption solution-processed strategy for the preparation of heterostructures of $MoSe_2$ nanosheet array on layered MoS_2, among which the two-dimensional MoS_2 surface is uniformly covered with high-density arrays of vertically aligned $MoSe_2$. The unique compositional and structural features of the MoS_2−$MoSe_2$ heterostructures not only provide more exposed active sites for sequent electrochemical process, but also facilitate the ion transfer due to the open porous space within the nanosheet array serving as well-defined ionic reservoirs. As a proof of concept, the MoS_2−$MoSe_2$ heterostructures serve as promising bifunctional electrodes for both energy conversions and storages, which exhibit an active and acid-stable activity for catalyzing the hydrogen evolution reaction, high specific capacity of 728 F g^{-1} at 0.1 A g^{-1}, and excellent durability with a remained capacity as high as 676 mA h g^{-1} after 200 cycles.

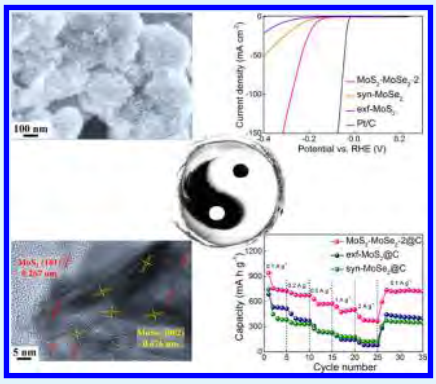

KEYWORDS: *transition-metal dichalcogenides, heterostructures, nanosheet array, hydrogen evolution reaction, lithium-ion batteries*

1. INTRODUCTION

Engineering heterostructures by combining different types of two-dimensional (2D) semiconductive materials with a preferred orientation have been regarded as a promising strategy tuning the electronic properties of 2D semiconductive materials with great potentials in energy storage and conversion,[1] catalysis,[2−4] electronics,[5−8] and sensing.[9] It is extremely effective to conduct a heterogeneous nucleation growth of transition metal dichalcogenides (TMDs) along the lateral or vertical directions of templates by tailoring semiconductive heterostructures with a well-defined interface.[10−13] Up to now, various 2D semiconductive heterostructures with nanoelements overlapping along their lateral direction have been developed by gas-phase deposition methods.[14−21] Although nanoelements in a vertical direction among the heterostructures could afford remarkable properties, such as strong interfacial interaction, low contacting resistance, and fast ion transport,[22−24] it is a great challenge to engineer different kinds of 2D semiconductive materials into heterostructures with nanoelements in a vertical direction especially using a low-cost and high-yield approach.[25−27]

Transition metal dichalcogenides (TMDs), such as MoS_2, $MoSe_2$, etc., have gained increasing attention due to their designable crystal structures and broad applications in energy applications.[27−33] The electrochemical performances of TMDs rely heavily on their lattice sizes, exposed crystalline phases, and compositional structures.[34−36] Bulk TMDs typically possess a lamellar crystal structure with weak van der Waals forces between layers and strong covalent bonding within each layers.[37,38] Therefore, the mechanical exfoliation of TMDs gives rise to a high-yield production of few-layer 2D nanoflakes of TMDs, which efficiently maintains the single crystalline nature for 2D TMDs.[39−41] Great efforts have currently been aspired to design high-performance epitaxial heterostructures for electrochemical applications.[1,40,42] The epitaxial heterostructures are usually derived from thermal chemical vapor deposition process with harsh technical requirements, high costs but low yields.[43] Regarding this, it would be a promising alternative to develop a solution-processed growth for TMD-based heterostructures, which would afford evident superiorities, including low cost, high throughout, ease of implementation, versatility, etc.[1,40,44]

Received: October 18, 2017
Accepted: December 1, 2017
Published: December 1, 2017

DOI: 10.1021/acsami.7b15854
ACS Appl. Mater. Interfaces 2017, 9, 44550−44559

With these perspectives, a simple, low-cost, and high-yield strategy is inspired for a solution-phase growth of vertically aligned $MoSe_2$ nanosheet array on layered MoS_2 to obtain the MoS_2−$MoSe_2$ heterostructures. Due to the unique compositional and structural features, the MoS_2−$MoSe_2$ heterostructures deliver the superior electrochemical activity and excellent durability for catalyzing the hydrogen evolution reaction (HER), and simultaneously exhibit excellent lithium ion storage properties with a remained capacity as high as 676 mA h g^{-1} after a long cycle extending to 200 cycles.

2. RESULTS AND DISCUSSION

The preparation of the vertically aligned MoS_2−$MoSe_2$ heterostructures was illustrated in Figure 1. Liquid-phase

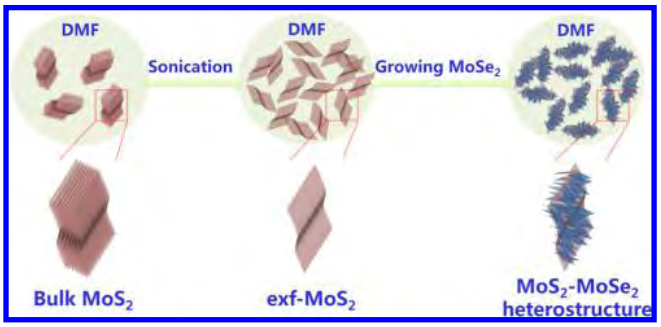

Figure 1. Schematic illustration of the synthesis route for vertically aligned MoS_2−$MoSe_2$ heterostructures.

sonication-assisted exfoliation of bulk MoS_2 in *N*,*N*-dimethylformamide produces a homogeneous high-concentration dispersion of exfoliated few-layer MoS_2 (exf-MoS_2). Upon sonication, the flake sizes of MoS_2 remarkably decrease, which would greatly increase the amounts of edge sulfur atoms.[37] The resultant exf-MoS_2 would easily get charged and stabilized in solvents due to the electrostatic repulsions between individual flakes. Afterward, a solvothermal growth is applied during which the exf-MoS_2 serves as a 2D template guiding the decoration and vertical alignment of the solverthermally synthesized $MoSe_2$ (syn-$MoSe_2$). After cooling down, the products were washed and dried, thus giving the MoS_2−$MoSe_2$ heterostructures. Inevitable aggregations of 2D MoS_2 and $MoSe_2$ materials would be simultaneously avoided due to the presence of the exf-MoS_2 template, and the syn-$MoSe_2$ nanosheet array would remain intact especially during the subsequent electrochemical processes.

The compositions of the well-defined MoS_2−$MoSe_2$ heterostructures were systematically verified by X-ray diffraction (XRD) and Raman spectroscopy. For Figure 2a, the diffraction patterns of exf-MoS_2 at 2θ = 14.4, 32.7, 39.5, 49.8, 58.3, and 60.2° can be assigned to the (002), (100), (103), (105), (110), and (008) planes, corresponding to hexagonal 2H-phase MoS_2 (JCPDF No. 65-1951).[27] Hexagonal 2H phase of syn-$MoSe_2$ can be clearly evidenced by the diffraction patterns at 13.1, 33.2, and 54.6°, which are respectively attributed to the (002), (100), and (110) planes of 2H-phase $MoSe_2$ (JCPDF No. 87-2419). The MoS_2−$MoSe_2$ heterostructures suggest the coexistence of hexagonal MoS_2 and $MoSe_2$ phases, indicating that the $MoSe_2$ nanosheets are successfully anchored on the exf-MoS_2 substrate. Moreover, the intensities of the diffraction peaks ascribing to the exf-MoS_2 gradually enhance with the increasing contents of exf-MoS_2 in the MoS_2−$MoSe_2$ heterostructures. Figure 2b displays the Raman spectra acquired from exf-MoS_2, syn-$MoSe_2$, and MoS_2-$MoSe_2$ heterostructures. For exf-MoS_2, the characteristic peaks observed at 376 and 402 cm^{-1} are corresponding to the in-plane E_{2g} and out-of-plane A_{1g} modes of hexagonal MoS_2, respectively. The separation (~26 cm^{-1}) between the $^1E_{2g}$ and A_{1g} modes reveals a few-layer structure of MoS_2. The characteristic peaks of syn-$MoSe_2$ are located at ~235 and 283 cm^{-1}, which are in agreement with $^1E_{2g}$ and A_{1g} of 2H-phase $MoSe_2$, respectively. The Raman spectrum of MoS_2−$MoSe_2$ heterostructures at a low frequency (100−500 cm^{-1}) consist of Mo−Se-related modes and Mo−S-related modes, indicating the successful construction of MoS_2−$MoSe_2$ heterostructures.

The compositions and binding energies of MoS_2−$MoSe_2$ heterostructures were further investigated by X-ray photoelectron spectroscopy (XPS) analysis. The survey XPS spectrum of MoS_2−$MoSe_2$-2 in Figure 2c reveals the coexistence of Mo, S, and Se elements in MoS_2−$MoSe_2$-2. High-resolution Mo 3d peak of MoS_2−$MoSe_2$-2 in Figure 2d exhibits two subpeaks at the binding energies of 229 and 232 eV, which are consistent with the doublet Mo $3d_{5/2}$ and Mo $3d_{3/2}$ orbitals, suggesting the formation of Mo^{4+}. These Mo 3d binding energies shift ~0.2 eV to lower binding energies than those of exf-MoS_2 and syn-$MoSe_2$, which are attributed to efficient electron transfer from $MoSe_2$ nanosheet array to MoS_2 substrates due to unique heterojunction effect.[45] Moreover, Se 3d peak with Se $3d_{5/2}$ and Se $3d_{3/2}$ orbitals at 54.3 and 55.4 eV, as well as Se $3p_{3/2}$ and Se $3p_{1/2}$ at 160 and 166.6 eV, respectively, is corresponding to the −2 oxidation state of Se within the heterostructures (Figure 2e). Figure 2f displays the enlarged S 2p spectra of MoS_2−$MoSe_2$-2, with S $2p_{1/2}$ and S $2p_{3/2}$ appearing at 161.2 and 162.6 eV, respectively. The Se/S molar ratio of MoS_2−$MoSe_2$-2 was calculated to be 0.695 based on the XPS results (see detailed derivation process in the Supporting Information). Moreover, thermal gravimetric analysis (TGA) measurements were also employed under air to determine the actual contents of exf-MoS_2 in the MoS_2−$MoSe_2$-1, MoS_2−$MoSe_2$-2, and MoS_2−$MoSe_2$-3. The TGA results measured in air flow were conducted to further estimate the actual contents of exf-MoS_2 in the MoS_2−$MoSe_2$ heterostructures (Figure S1). Notably, the weight increases between 200 and 320 °C can be observed in the MoS_2−$MoSe_2$ heterostructures as well as neat $MoSe_2$, which can be ascribed to the formation of SeO_2 during the oxidation of $MoSe_2$ into MoO_3. An increase in temperature causes an obvious weight loss due to the gasification of SeO_2. The final residues of MoO_3 for MoS_2−$MoSe_2$-1, MoS_2−$MoSe_2$-2, and MoS_2−$MoSe_2$-3 are 80.6, 74.3, and 68.7%, respectively. Considering the final residues of MoS_2 and $MoSe_2$ are 83.6 and 57.3%, respectively, the actual weight percentages of the exf-MoS_2 within MoS_2−$MoSe_2$-1, MoS_2−$MoSe_2$-2, and MoS_2−$MoSe_2$-3 are calculated to be 54.9, 64.6, and 77.6%, respectively.

The morphologies of MoS_2−$MoSe_2$ heterostructures were investigated by scanning electron microscopy (SEM) and transmission electron microscopy (TEM) observations. SEM images of exf-MoS_2 in Figure 3a display well-exfoliated layers with small number of stacked 2D nanoflakes. TEM images of exf-MoS_2 in Figure S2a,b indicate that the lateral sizes of exf-MoS_2 distribute ranging from 50 to 200 nm, and the exf-MoS_2 edges can be observed with less than six layers. The SEM images of neat $MoSe_2$ in Figure S3a,b manifest a nanoflower morphology assembled by curved $MoSe_2$ nanosheets. Typical

DOI: 10.1021/acsami.7b15854
ACS Appl. Mater. Interfaces 2017, 9, 44550−44559

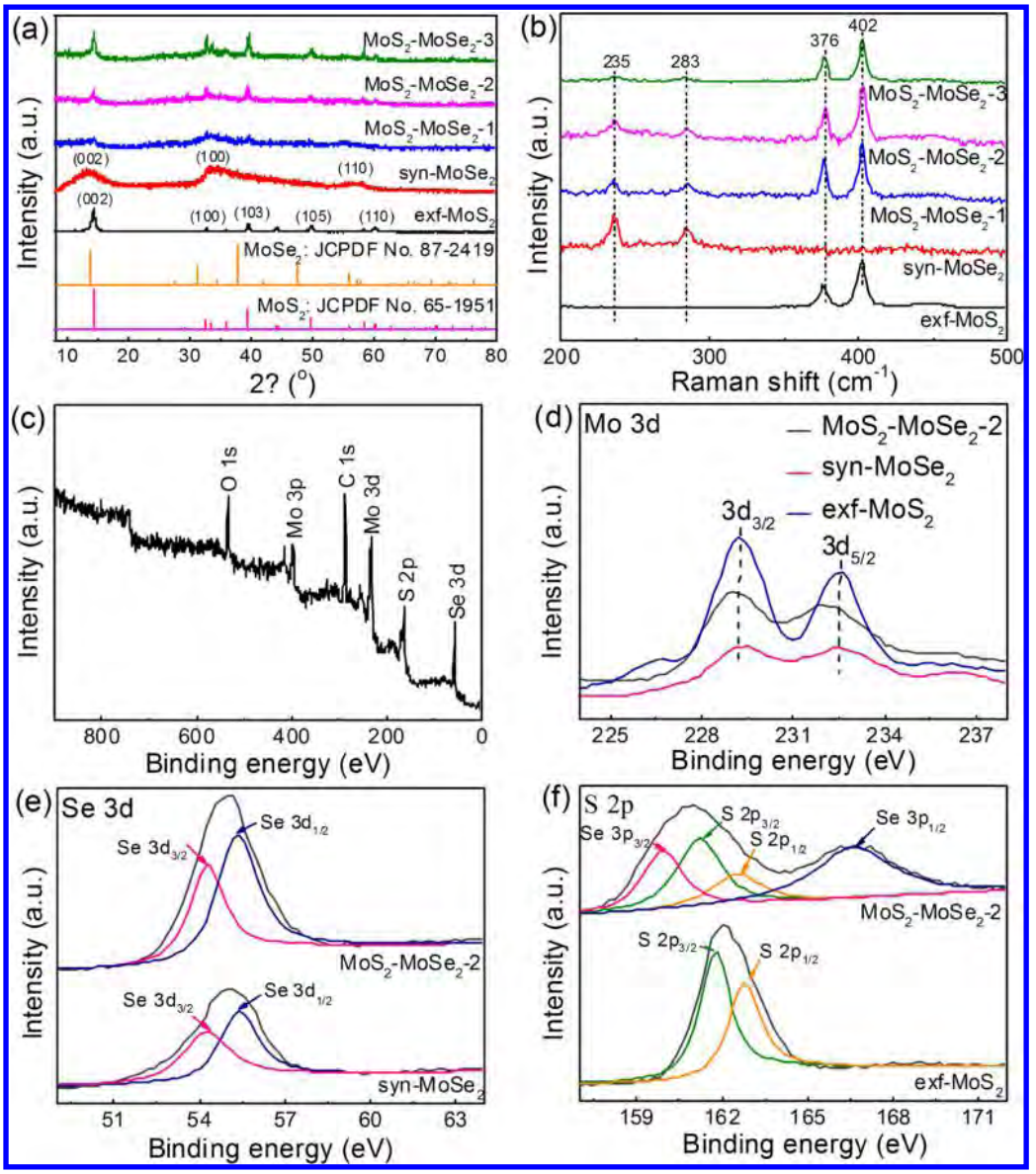

Figure 2. (a) XRD patterns, (b) Raman spectra, and X-ray photoelectron spectroscopy (XPS) spectra of exf-MoS_2, syn-$MoSe_2$, and MoS_2−$MoSe_2$-2: (c) survey spectrum, (d) Mo 3d, (e) Se 3d, and (f) S 2p.

TEM images (Figure S3c,d) indicate that neat $MoSe_2$ nanoflowers are composed of ultrathin nanosheets with an interlayer spacing of ~0.65 nm. For MoS_2−$MoSe_2$-2 (Figure 2b,c), vertically aligned $MoSe_2$ nanosheet arrays are perpendicularly anchored on the surface of exf-MoS_2 without any agglomeration and restacking, and plentiful nanopores of 20−50 nm appear in the nanosheet array network formed by wrinkled $MoSe_2$ nanosheets, which would provide multiple transport channels promoting ion diffusions of electrolyte. TEM images of MoS_2−$MoSe_2$-2 (Figure 2d,e) clearly point out that exf-MoS_2 templates are completely covered by the interconnected $MoSe_2$ nanosheet arrays. The lattice fringe of exf-MoS_2 and few-layer $MoSe_2$ (3−10 layers) can be distinctly noticed from the high-resolution transmission electron microscopy (HRTEM) image of MoS_2−$MoSe_2$-2 in Figure 2f. Energy-dispersive X-ray spectroscopy results reveal the coexistence and homogeneous distribution of Mo, S, and Se elements in MoS_2−$MoSe_2$-2, indicating a uniform growth of syn-$MoSe_2$ on exf-MoS_2 substrates. The effects of the contents of exf-MoS_2 substrates on the microstructures of MoS_2−$MoSe_2$ heterostructures were systematically investigated. For MoS_2−$MoSe_2$-1 prepared with fewer MoS_2 templates, the density of $MoSe_2$ nanosheets on exf-MoS_2 clearly increases (Figure S4a,b). Dense $MoSe_2$ nanosheet agglomerates form with decreased contents of MoS_2 substrates within MoS_2−$MoSe_2$-1, indicating that excessive $MoSe_2$ aggregates gradually deposit on the surface of exf-MoS_2 substrates due to insufficient exf-MoS_2 substrates. Whereas for MoS_2−$MoSe_2$-3 prepared with excess MoS_2 substrates, only few $MoSe_2$ nanosheets are found and selectively grown on some of exf-MoS_2 substrates, and a great deal of exf-MoS_2 substrates are uncovered (Figure S4c,d). Therefore, the vertically aligned MoS_2−$MoSe_2$ heterostructures constructed with diverse heteroelements can be easily tuned by simply adjusting the amounts of the exf-MoS_2 substrates. Among the vertically aligned MoS_2−$MoSe_2$ heterostructures, the aggregation of exf-MoS_2 and syn-$MoSe_2$ can be simultaneously avoided due to a synergistic dispersion.

DOI: 10.1021/acsami.7b15854
ACS Appl. Mater. Interfaces 2017, 9, 44550−44559

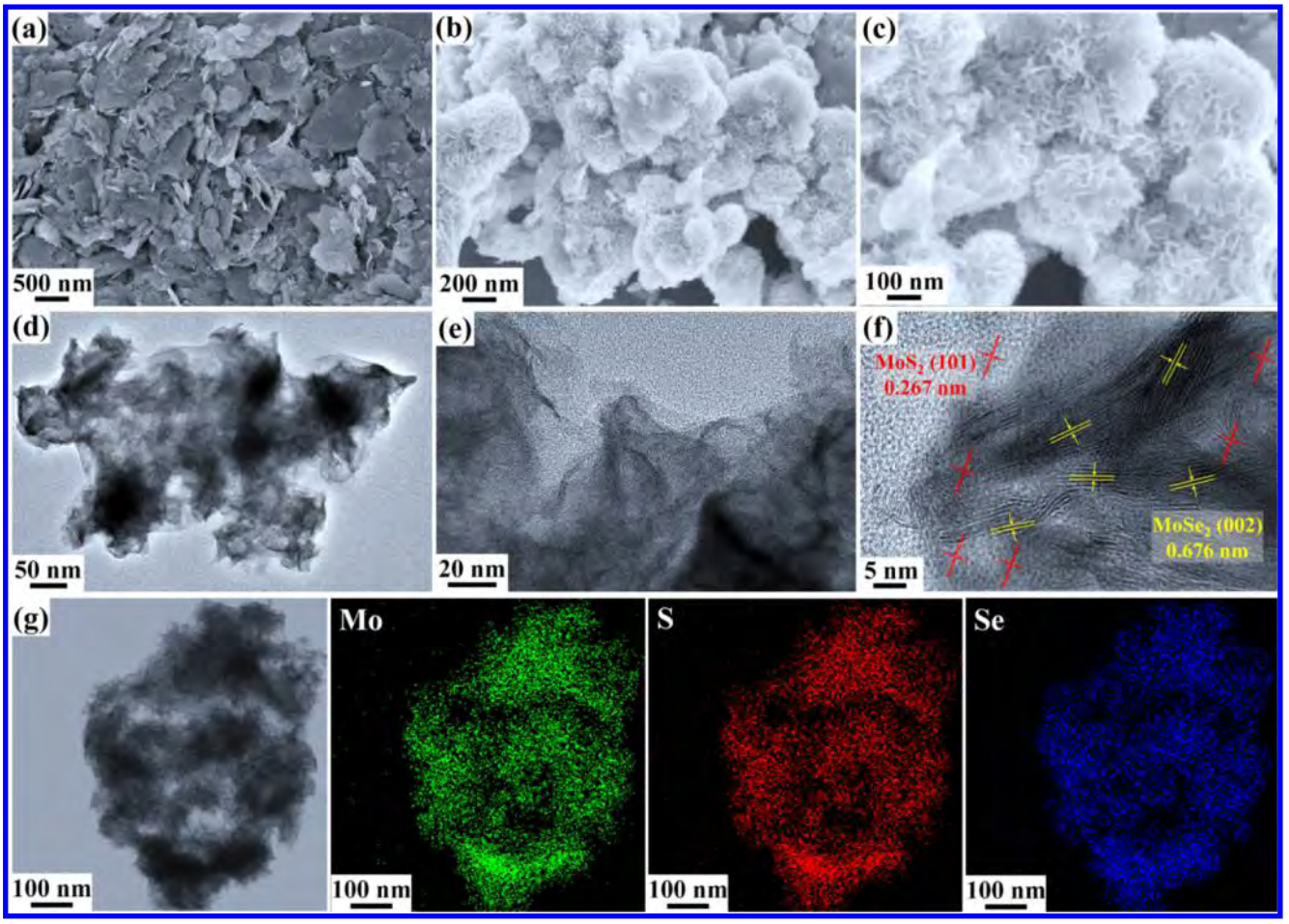

Figure 3. SEM images of (a) exf-MoS_2 and (b, c) MoS_2−$MoSe_2$-2 at low and high magnifications, respectively. TEM images of MoS_2−$MoSe_2$-2 at (d) low and (e) high magnifications, respectively. (f) HRTEM image of MoS_2−$MoSe_2$-2 indicating the crystal planes of MoS_2 and $MoSe_2$, respectively. (g) TEM image of MoS_2−$MoSe_2$-2 and corresponding elemental mappings of Mo, S, and Se.

Vertical growth of $MoSe_2$ nanosheets on exf-MoS_2 can efficiently enhance the exposure of highly active sites and provide the porous network with a large surface area, which can efficiently accelerate the electron transfer and shorten the diffusion pathway of ions. Electrochemical HER performances were evaluated by using a three-electrode setup in N_2-saturated 0.5 M H_2SO_4 electrolyte. Figure 4a presents the polarization curves of MoS_2−MoS_2 heterostructures compared with exf-MoS_2, syn-$MoSe_2$, and commercially available Pt/C catalyst at a scan rate of 2 mV s^{-1}. Neat exf-MoS_2 electrode exhibits an overpotential of 338 mV at a current density of 10 mA cm^{-2}, which shows a slightly increased catalytic activity compared with bulk MoS_2 electrode due to more exposed active sites generated by exfoliation (Figure S5). Neat syn-$MoSe_2$ electrode requires an overpotential of 240 mV to achieve the current density of 10 mA cm^{-2}. After hybridizing syn-$MoSe_2$ with exf-MoS_2, MoS_2−$MoSe_2$-2 exhibits optimized HER catalytic activity with a small overpotential of 175 mV at 10 mA cm^{-2}, superior to MoS_2−$MoSe_2$-1 (208 mV) and MoS_2−$MoSe_2$-3 (182 mV), which are attributed to more exposed catalytic active sites with uniformly immobilized syn-$MoSe_2$ on exf-MoS_2 templates. Within the MoS_2−$MoSe_2$-1 sample, excess syn-$MoSe_2$ nanosheets, which aggregate into nanoflowers, inherently restrict the ion diffusion and electron transfer for water splitting. For MoS_2−$MoSe_2$-3, excess exf-MoS_2 with poor intrinsic catalytic activities results in scare active sites toward hydrogen atom adsorption as well as weakened HER performance. It should be noted that all of the linear sweep voltammetry (LSV) curves have been repeated at least three times, and these polarization curves of the MoS_2−$MoSe_2$-2 electrodes exhibit great reproducibility (Figure S6).

Ultrathin carbon coating is performed through a hydrothermal carbonization followed by a high-temperature pyrolysis to further enhance the electrical conductivity of the resultant MoS_2−$MoSe_2$ heterostructures.[46] The ultrathin carbon-coated exf-MoS_2, syn-$MoSe_2$, and MoS_2−$MoSe_2$-2 are denoted as exf-MoS_2@C, syn-$MoSe_2$@C, and MoS_2-$MoSe_2$-2@C, respectively. The SEM and TEM images of the MoS_2−$MoSe_2$-2@C were characterized and are shown in Figure S7. The vertical alignment of the $MoSe_2$ nanosheets on the MoS_2 substrate still maintains upon the carbon coating. Furthermore, we also investigate the electrochemical properties of MoS_2−$MoSe_2$-2@C and MoS_2−$MoSe_2$-2 with carbon black additives to identify the influence of the electrical conductivities of the catalysts on the final HER performance. Figure S8 compares the LSV curves of MoS_2−$MoSe_2$-2, MoS_2−$MoSe_2$-2 with carbon black additives, and MoS_2−$MoSe_2$-2@C. The MoS_2−$MoSe_2$-2 electrode with carbon black additives presents an improved catalytic activity with a low overpotential of 154 mV at 10 mA cm^{-2} when compared with neat MoS_2−$MoSe_2$-2, indicating that the carbon black additives could promote fast electron transfer, thus boosting the electrocatalytic properties. However,

DOI: 10.1021/acsami.7b15854
ACS Appl. Mater. Interfaces 2017, 9, 44550−44559

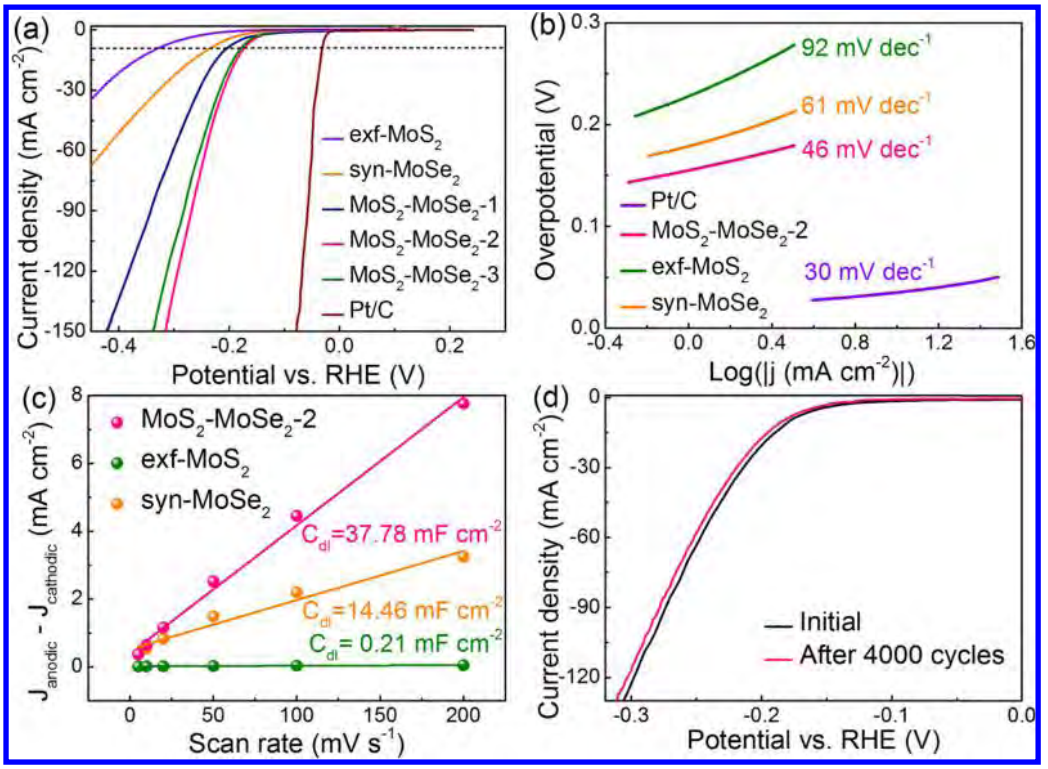

Figure 4. (a) Polarization curves of MoS_2−$MoSe_2$ heterostructures compared with exf-MoS_2, syn-$MoSe_2$, and Pt/C at a scan rate of 2 mV s^{-1} in a N_2-purged 0.5 M H_2SO_4 electrolyte. (b) The corresponding Tafel plots from the polarization curves with a scan rate of 0.5 mV s^{-1} for MoS_2−$MoSe_2$ heterostructures, exf-MoS_2, and syn-$MoSe_2$. (c) Linear fitting of capacitive current densities against scan rates of MoS_2−$MoSe_2$-2, exf-MoS_2, and syn-$MoSe_2$. (d) Polarization curves of MoS_2−$MoSe_2$-2 electrode initially and after 4000 cycles between −0.4 and 0.2 V vs reversible hydrogen electrode (RHE) at a scan rate of 50 mV s^{-1}.

the electrochemical HER activity of the MoS_2−$MoSe_2$-2@C electrode is decreased clearly with a high overpotential of 214 mV at 10 mA cm^{-2}, which can be ascribed to the reason that carbon coating on the surface of MoS_2−$MoSe_2$ heterostructures will lead to the encapsulation of active sites and thus reduce the number of exposed active sites.

The HER kinetics of catalysts is further explored by Tafel plots stemming from the corresponding LSV curves. The Tafel slopes were obtained from the linear portions of Tafel plots according to the Tafel equation: $\eta = b\log(j) + a$, where η, b, and j represent the overpotential, Tafel slope, and current density, respectively.[47] Figure 4b indicates that the Pt/C electrode shows the best HER catalytic performance with a small overpotential of 32 mV at 10 mA cm^{-2}. The MoS_2−$MoSe_2$-2 electrode exhibits the lowest Tafel slope of 46 mV dec^{-1}, whereas syn-$MoSe_2$ and exf-MoS_2 electrodes exhibit higher Tafel slopes of 61 and 92 mV dec^{-1}, respectively. Typically, the generation of hydrogen involves three reaction steps, including Volmer (~120 mV dec^{-1}), Heyrovsky (~40 mV dec^{-1}), and Tafel (~30 mV dec^{-1}) reactions.[48] Therefore, the Tafel slope values mentioned above for all of the electrodes demonstrate that Volmer−Heyrovsky mechanism comes into effect during the electrochemical process. Furthermore, lower Tafel slope theoretically reveals faster HER kinetics, that is, the catalyst is required to apply a lower overpotential to produce a higher current density. Hence, MoS_2−$MoSe_2$-2 electrode with a smaller Tafel slope and a higher current density at the designed overpotentials presents the optimal catalytic activity with superior H_2 evolving efficiency. The charge transfer resistance (R_{ct}) values of the MoS_2−$MoSe_2$-2, syn-$MoSe_2$, and exf-MoS_2 electrodes, which are determined by conducting the electrochemical impedance spectroscopy (EIS) curves at an overpotential of 210 mV, are estimated to be ~122, 148, and 175 Ω, respectively (Figure S9). In general, R_{ct} is related to the electrocatalytic reaction rate, and a lower R_{ct} value indicates faster catalytic kinetics.[45] Therefore, the lower R_{ct} value of the MoS_2−$MoSe_2$-2 electrode reveals a rapider charge transfer process between the interfaces of electrode and electrolyte. The heterointerfaces between the exf-MoS_2 substrate and vertically anchored $MoSe_2$ nanosheets also facilitate the charge transfer and modulate the electronic structure, thus increasing the conductivity of the MoS_2−$MoSe_2$-2 electrode.

To analyze the influence of the enhanced active sites and specific surface areas on the final HER activity, nitrogen adsorption/desorption isotherms and pore size distributions of MoS_2−$MoSe_2$-2, exf-MoS_2, and syn-$MoSe_2$ were measured and are provided in Figure S10. The specific surface areas of MoS_2−$MoSe_2$-2, exf-MoS_2, and syn-$MoSe_2$ were calculated to be 32, 17.4, and 19.5 m^2 g^{-1}, respectively. The MoS_2−$MoSe_2$-2 structures possess an enlarged pore volume with both micropores and mesopores, and the improved specific surface areas and pore volume could result in enhanced HER activity of MoS_2−$MoSe_2$-2. Moreover, the electrochemical double-layer capacitances (C_{dl}) were measured to further evaluate the electrochemical active surface area of catalysts. Cyclic voltammetry (CV) at different scan rates of 5, 10, 20, 50, 100, and 200 mV s^{-1} during the potential range of 0.1−0.2 V vs RHE was performed (Figure S11). The current density variation ΔJ ($\Delta J = J_{anodic} - J_{cathodic}$) at 0.15 V vs RHE is plotted as a function with different scan rates, and the half of the slope is considered to be the estimation of C_{dl} value, as depicted in Figure 4c.[49] The MoS_2−$MoSe_2$-2, syn-$MoSe_2$, and

DOI: 10.1021/acsami.7b15854
ACS Appl. Mater. Interfaces 2017, 9, 44550−44559

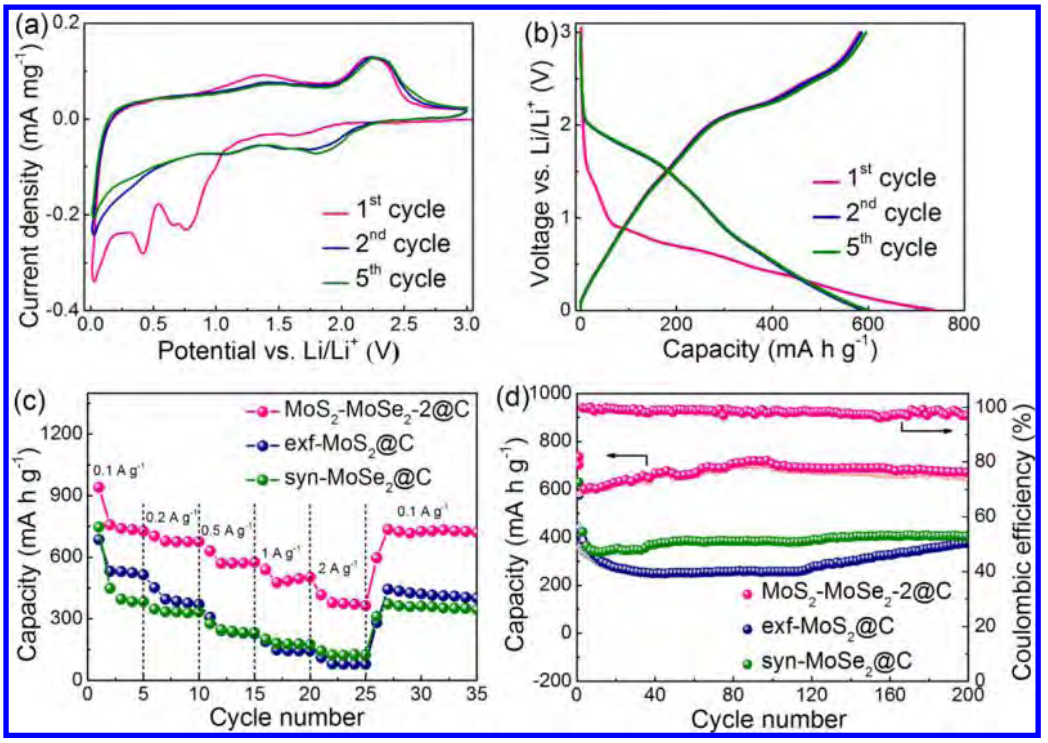

Figure 5. Electrochemical performances of MoS_2−$MoSe_2$-2@C, exf-MoS_2@C, and syn-$MoSe_2$@C electrodes for LIBs. (a) CV profiles of MoS_2−$MoSe_2$-2@C at a scan rate of 0.1 mV s^{-1}. (b) Galvanostatic charge/discharge profiles of MoS_2−$MoSe_2$-2@C at a current density of 0.2 A g^{-1}. (c) Rate capabilities of MoS_2−$MoSe_2$-2@C, exf-MoS_2@C, and syn-$MoSe_2$@C electrodes at different current densities. (d) Cycling behavior of MoS_2−$MoSe_2$-2@C, exf-MoS_2@C, and syn-$MoSe_2$@C electrodes at a current density of 0.2 A g^{-1}.

exf-MoS_2 electrodes generate the capacitance value of 37.78, 14.46, and 0.21 mF cm^{-2}, respectively, suggesting that the hybridization of MoS_2 and $MoSe_2$ leads to more exposed active sites and increased effective electrochemical active surface area. The CV curves of the exf-MoS_2, syn-$MoSe_2$, and MoS_2−$MoSe_2$-2 electrodes were recorded in the range of −0.4 to 0.6 V (vs RHE) in a phosphate buffer saline (PBS) electrolyte (pH = 7) with a scan rate of 50 mV s^{-1} to directly investigate the turnover frequency (TOF) of each active site (Figure S12). The number of active sites was determined to be 1.11 × 10^{-6} mol for MoS_2−$MoSe_2$-2, higher than that of exf-MoS_2 (0.98 × 10^{-6} mol) and syn-$MoSe_2$ (1.08 × 10^{-6} mol). What is more, the TOF of H_2 molecules evolved per second for the MoS_2−$MoSe_2$-2, exf-MoS_2, and syn-$MoSe_2$ electrodes was calculated to be 7.53 × 10^{-3}, 0.29 × 10^{-3}, and 1.51 × 10^{-3} s^{-1} at η = 200 mV, respectively, manifesting that MoS_2−$MoSe_2$-2 possesses a higher intrinsic catalytic activity for HER.

Long-cycle durability of catalysts is also regarded as a significant descriptor to assess the HER activity for their practical applications. Continuous CV scans between −0.4 and 0.2 V vs RHE were carried out for 4000 cycles at a scan rate of 50 mV s^{-1}. The typical time dependence of the current density of the MoS_2−$MoSe_2$-2 electrode was also conducted under a static overpotential of ∼200 mV. Negligible decay of onset potential and current density can be observed from the LSV plots (Figure 4d) and I−t curves (Figure S13), manifesting that MoS_2−$MoSe_2$-2 is a durable catalyst to bear accelerated degradations in acidic media, and the slight deterioration might be aroused by the consumption of H^+ and the accumulation of H_2 bubbles around the electrode surface, which would hinder the electrochemical reaction.[50] The SEM images of the MoS_2−$MoSe_2$-2 electrode after cycling were characterized. Figure S14 shows that the vertical alignment of the MoS_2−$MoSe_2$ heterostructures maintains well after cycling, indicating the superior structural stability of the MoS_2−$MoSe_2$ heterostructures for HER. The exceptional durability can be attributed to the strong heterogeneous interactions between MoS_2 and $MoSe_2$, which display prospective practical applications.

As another proof-of-concept application, the unique structural characteristics of MoS_2−$MoSe_2$ heterostructures, including porous void structure stacked of ultrathin nanosheets and good structural robustness, make it a promising anode material for lithium ion batteries (LIBs). The electrochemical performances of exf-MoS_2@C, syn-$MoSe_2$@C, and MoS_2−$MoSe_2$-2@C for reversible Li^+ storage were probed by CV and galvanostatic charge/discharge measurements in Figures 5 and S15. The initial five CV profiles of MoS_2−$MoSe_2$-2@C electrode measured at a scan rate of 0.2 mV s^{-1} in the voltage range of 0.01−3 V vs Li/Li$^+$ are shown in Figure 5a. Only two board cathodic peaks for MoS_2−$MoSe_2$-2@C electrode are centered at ∼0.76 and 0.4 V during the first lithiation process, which may be attributed to the similar reduction reaction of exf-MoS_2@C (0.86/0.38 V in Figure S15a) and syn-$MoSe_2$@C (0.83/0.34 V in Figure S15c) due to their similar structures. The first cathodic peak at 0.76 V corresponds to the lithiation reaction with Li^+ ions inserted into the layer-to-layer space of MoS_2 or $MoSe_2$ to form Li_xMoS_2 or Li_xMoSe_2. The discharge plateau at 0.4 V can be assigned to a conversion reaction process, which first entails the in situ decomposition of Li_xMoS_2 or Li_xMoSe_2 into Mo particles embedded in a Li_2S or Li_2Se matrix, together with the formation of a polymeric gel-like layer resulting from the electrochemically activated electrolyte degradation. The overall lithium insertion process could be described as follows: $MoS_2 + 4Li^+ \rightarrow Mo + 2Li_2S$, $MoSe_2 + 4Li^+ \rightarrow Mo + 2Li_2Se$. In the subsequent lithiation process, two

DOI: 10.1021/acsami.7b15854
ACS Appl. Mater. Interfaces 2017, 9, 44550−44559

reduction peaks appear at around 1.8 and 1.1 V, and the peak at about 0.76 V in the first discharge process disappears, which is in accordance with the reported lithiation behaviors of MoS_2 and $MoSe_2$. Upon the first and subsequent charging process, a stable anodic peak at approximately 2.2 V can be clearly identified for the oxidation reaction of Mo to MoS_2 or $MoSe_2$, which simultaneously indicates the excellent stability of MoS_2−$MoSe_2$-2@C electrode during the lithiation and delithiation process. Furthermore, these redox peaks of CV curves can be corresponding with the potential plateaus observed from the related charge/discharge curves in Figures 5b and S15b,d. Meanwhile, calculated from the galvanostatic charge/discharge curves, a discharge specific capacity of 1144 mA h g^{-1} for MoS_2−$MoSe_2$-2@C during the first intercalation process and a corresponding charge capacity of 895 mA h g^{-1} are reversibly recovered, thus achieving a Coulombic efficiency of 78.2%. The irreversible capacity loss is commonly ascribed to the formation of solid electrolyte interface (SEI) on the fresh electrode surface or a small amount of some lithium trapping inside the defects and disorder structures.[51−53] However, the first discharge and charge capacities of exf-MoS_2@C electrode are 1103 and 766 mA h g^{-1}, respectively, with a Coulombic efficiency of only 69.7% (Figure S15a), which is much higher than the theoretical capacity of bulk MoS_2 (167 mA h g^{-1}).[54] Figure S15c also displays that at the first discharge/charge cycle, syn-$MoSe_2$@C electrode achieves an initial discharge capacity of 960 mA h g^{-1} and the corresponding charge capacity of 694 mA h g^{-1}, which means the initial Coulombic efficiency is 72.3%. Furthermore, we also investigate the electrochemical behaviors of neat carbon by CV and galvanostatic charge/discharge measurements (Figure S18). No redox peaks and voltage plateau can be observed for neat carbon as an anode material for LIBs during the electrochemical process.

Benefiting from the attractive heterostructures, MoS_2−$MoSe_2$-2@C manifests great rate capacity and cycling performance, as described in Figure 5c,d. With the current density increasing from 0.1 to 0.2, 0.5, and 1 A g^{-1}, the discharge capacity of MoS_2−$MoSe_2$-2@C electrode slowly decreases from 728 to 676, 573, and 496 mA h g^{-1}, which is much better than that of syn-$MoSe_2$@C and exf-MoS_2@C electrodes. Even at large current density of 2 A g^{-1}, the discharge capacity of 375 mA h g^{-1} can still be retained for the MoS_2−$MoSe_2$-2@C electrode. Such an excellent rate behavior of the MoS_2−$MoSe_2$-2@C electrode can be also proved by the reversible capacity recovery after cycling. When current density returns to 0.1 A g^{-1}, an increased discharge capacity for MoS_2−$MoSe_2$-2@C is recovered up to 736 mA h g^{-1}. However, the syn-$MoSe_2$@C and exf-MoS_2@C electrodes only deliver the discharge capacities of 362 and 444 mA h g^{-1}, respectively, when the current density returns to 0.1 A g^{-1}. Moreover, the superior rate performance and high reversible capacity of MoS_2−$MoSe_2$@C electrode can be also evidenced by the cycling stability. Figure 5d presents the charge/discharge capacities over cycling at a current density of 0.2 A g^{-1} for MoS_2−$MoSe_2$-2@C, syn-$MoSe_2$@C, and exf-MoS_2@C electrodes, together with the Coulombic efficiency of the MoS_2−$MoSe_2$@C electrode. The first discharge and charge capacities of MoS_2−$MoSe_2$-2@C are found to be ∼736 and 581 mA h g^{-1}, respectively. The irreversible specific capacity loss of 78.9% may be mainly ascribed to the formation of solid electrolyte interfaces (SEIs) and electrolyte decomposition, which is a common phenomenon in most anode materials. In the subsequent cycles, the continued reversible capacity increase can be observed from 581 mA h g^{-1} to a high level of 721 mA h g^{-1} during the first 100 cycles, and then a stable capacity of ∼680 mA h g^{-1} can be maintained constant with a high Coulombic efficiency above 98%. Such a capacity rising with cycling can be attributed to the activation of active materials and the reversible growth of organic polymeric gel-like layers resulting from kinetically activated electrolyte degradation.[55−58] Theoretically, the polymeric gel-like layers on active materials ensure the mechanical cohesion and deliver excess capacity at low potential through the so called "pseudo-capacitance-type behavior".[59,60] To demonstrate the superiority of MoS_2−$MoSe_2$ heterostructures on lithium storages, the cycling behaviors of syn-$MoSe_2$@C and exf-MoS_2@C were also examined under the same conditions. The syn-$MoSe_2$@C and exf-MoS_2@C electrodes deliver an initial discharge capacity of 482 and 410 mA h g^{-1}, respectively, with only 404 and 371 mA h g^{-1} reversible capacities retained after 200 cycles. Electrochemical impedance spectroscopy (EIS) measurement was also implemented to further understand the charge-transfer mechanism and enhanced electrochemical performance of the MoS_2−$MoSe_2$@C electrode (Figure S16). The semicircle in the high-frequency region of Nyquist plot represents the charge transfer resistance (R_{ct}) of electrode/electrolyte interface. A lower R_{ct} value indicates faster electrocatalytic kinetics. The R_{ct} of MoS_2−$MoSe_2$-2@C electrode is ∼66 Ω, which is remarkably lower than that of syn-$MoSe_2$@C (129 Ω) and exf-MoS_2@C (145 Ω), manifesting that the distinct combination of MoS_2 and $MoSe_2$ efficiently promotes the migration of Li ions and penetration of electrolytes for excellent lithium storage performance.

With the aim of confirming the merits of highly conductive carbon coatings on the MoS_2−$MoSe_2$ electrodes on lithium storage, the rate capacity, cycling performance, and EIS spectra of MoS_2−$MoSe_2$-2 and MoS_2−$MoSe_2$-2@C are examined under the same condition. As exhibited in Figure S17, compared with MoS_2−$MoSe_2$-2@C electrode, a faster capacity fading with continuously increasing current densities can be observed for MoS_2−$MoSe_2$-2 electrode. The reversible discharge capacity of only 448 mA h g^{-1} for MoS_2−$MoSe_2$-2 electrode can be restored when current density returns back to low current density of 0.1 A g^{-1}, which is significantly lower than that of the MoS_2−$MoSe_2$@C electrode (736 mA h g^{-1}). Moreover, rapid capacity loss is also discovered through cycling for the MoS_2−$MoSe_2$-2 electrode. Typically, MoS_2−$MoSe_2$ electrode suffers from a rapid capacity loss during the initial 70 cycles, and then delivers a stable but extremely low capacity of 187 mA h g^{-1}. Such a severe attenuation indicates the drastic volume expansion and grievous collapse of MoS_2−$MoSe_2$-2 structures without the protection of carbon layers. The rate capacity and cycling performance of neat carbon were also tested and are exhibited in Figure S18c,d. With a stepwise increase in the current densities, the reversible capacities of 244, 171, 103, and 58 mA h g^{-1} for neat carbon at 0.1, 0.2, 0.5, and 1 A g^{-1}, respectively, were achieved, which are much lower than those of the MoS_2−$MoSe_2$-2@C electrode under the corresponding current density. Figure S18d indicates that the neat carbon electrode possesses a good cyclic performance with a reversible capacity of ∼220 mA h g^{-1} at 0.2 A g^{-1} after 200 charge/discharge cycles. The carbon layers around the MoS_2−$MoSe_2$ heterostructures may act as a buffering layer cushioning the internal strain and preventing the active material from being electrically isolated during the electrochemical lithium proc-

DOI: 10.1021/acsami.7b15854
ACS Appl. Mater. Interfaces 2017, 9, 44550−44559

ess.[61,62] Furthermore, due to the existence of a conductive carbon layer, our MoS_2−$MoSe_2$-2@C electrode presents much lower R_{ct} of 66 Ω than that of MoS_2−$MoSe_2$-2 (141 Ω) (Figure S17c).

The optimized electrochemical properties of MoS_2−$MoSe_2$ heterostructures for HER and LIBs are probably related to their unique compositional and structural characteristics. First, the porous space derived from neighboring 2D $MoSe_2$ within the nanosheet array could afford shorted diffusion channels for lithium or hydrogen ions with an optimized interface between electrode and electrolytes. Second, the MoS_2−$MoSe_2$ heterostructures could provide an edge-to-edge configuration with more exposed active sites for both HER and lithium storages. Third, the heterostructures with a coupling of p-type $MoSe_2$ and n-type MoS_2 with matched energy levels could achieve a high-quality heterointerface within the heterostructures, which can facilitate a fast interfacial charge transfer and give rise to improved electrochemical activity and efficiency.[63]

3. CONCLUSIONS

In summary, we have explored a low-cost and high-yield strategy to construct heterostructures of $MoSe_2$ nanosheet array on layered MoS_2 as a bifunctional electrode with potential applications in water electrolyzers and anodes for LIBs. The resultant MoS_2−$MoSe_2$ heterostructures deliver outstanding HER performance with an overpotential of 175 mV at 10 mA cm^{-2} and a small Tafel slope of 46 mV dec^{-1}, and a long-term durability after 4000 cycles. When evaluated as anodes for LIBs, the MoS_2−$MoSe_2$ heterostructures deliver high Coulombic efficiency above 98%, high specific capacity of 728 mA h g^{-1} at 0.1 A g^{-1}, and excellent cycling performance maintaining 676 mA h g^{-1} after 200 cycles. This is strongly related to the unique MoS_2−$MoSe_2$ heterostructures with a vertically aligned sheet-on-sheet configuration, leading to improved mass transport and excellent electrical conductivity. The presented solution-processed strategy for the construction of vertically aligned TMD heterostructures may provide a new insight for the development of high-performance and durable electrodes for both energy conversation and storage applications.

ASSOCIATED CONTENT

Supporting Information

The Supporting Information is available free of charge on the ACS Publications website at DOI: 10.1021/acsami.7b15854.

TGA curves of MoS_2−$MoSe_2$-1, MoS_2−$MoSe_2$-2, and MoS_2−$MoSe_2$-3; TEM images of exf-MoS_2 and syn-$MoSe_2$; SEM images of syn-$MoSe_2$, MoS_2-$MoSe_2$-1, and MoS_2-$MoSe_2$-3; SEM and TEM images of MoS_2−$MoSe_2$-2@C; polarization curves of bulk MoS_2 and exf-MoS_2; comparison of polarization curves of MoS_2−$MoSe_2$@C, MoS_2−$MoSe_2$-2, and MoS_2−$MoSe_2$-2 with carbon black; polarization curves of the MoS_2−$MoSe_2$-2 electrode prepared in different batches; nitrogen adsorption/desorption isotherms and pore size distributions of MoS_2−$MoSe_2$-2, exf-MoS_2, and syn-MoS_2; CV curves of exf-MoS_2, syn-$MoSe_2$, and MoS_2−$MoSe_2$-2 electrodes; CV curves of exf-MoS_2, syn-$MoSe_2$, and MoS_2−$MoSe_2$-2 electrodes recorded in a PBS electrolyte; Nyquist plots of the exf-MoS_2, syn-$MoSe_2$, and MoS_2−$MoSe_2$-2 electrodes; time dependence of the current density of MoS_2−$MoSe_2$-2 electrode at an overpotential of 200 mV; SEM images of the MoS_2−$MoSe_2$-2 after the cycling stability test; CV profiles and galvanostatic charge/discharge profiles of exf-MoS_2 and syn-$MoSe_2$ electrodes; Nyquist plots of exf-MoS_2@C, syn-$MoSe_2$@C, and MoS_2−$MoSe_2$-2@C electrodes; the rate capabilities at different current densities, cycling behavior, and Nyquist plots of MoS_2−$MoSe_2$-2@C and MoS_2−$MoSe_2$-2; the electrochemical performances of neat carbon prepared through a hydrothermal carbonization followed by a high-temperature pyrolysis (PDF)

AUTHOR INFORMATION

Corresponding Authors

*E-mail: czhang@dhu.edu.cn (C.Z.).
*E-mail: txliu@dhu.edu.cn, txliu@fudan.edu.cn (T.L.).

ORCID

Jixin Zhu: 0000-0001-8749-8937
Jingsan Xu: 0000-0003-1172-3864
Tianxi Liu: 0000-0002-5592-7386

Notes

The authors declare no competing financial interest.

ACKNOWLEDGMENTS

We are grateful for the financial support from the National Natural Science Foundation of China (51433001, 21504012, 51773035, and 21501091), the Program of Shanghai Subject Chief Scientist (17XD1400100), the Natural Science Foundation of Shanghai (17ZR1439900), the Fundamental Research Funds for the Central Universities (17D110606).

REFERENCES

(1) Huang, X.; Zeng, Z.; Bao, S.; Wang, M.; Qi, X.; Fan, Z.; Zhang, H. Solution-phase epitaxial growth of noble metal nanostructures on dispersible single-layer molybdenum disulfide nanosheets. *Nat. Commun.* **2013**, *4*, No. 1444.

(2) Komanicky, V.; Iddir, H.; Chang, K.-C.; Menzel, A.; Karapetrov, G.; Hennessy, D.; Zapol, P.; You, H. Shape-dependent activity of platinum array catalyst. *J. Am. Chem. Soc.* **2009**, *131*, 5732−5733.

(3) Enterkin, J. A.; Poeppelmeier, K. R.; Marks, L. D. Oriented catalytic platinum nanoparticles on high surface area strontium titanate nanocuboids. *Nano Lett.* **2011**, *11*, 993−997.

(4) Habas, S. E.; Lee, H.; Radmilovic, V.; Somorjai, G. A.; Yang, P. Shaping binary metal nanocrystals through epitaxial seeded growth. *Nat. Mater.* **2007**, *6*, 692−697.

(5) Costi, R.; Saunders, A. E.; Banin, U. Kolloidale Hybrid-nanostrukturen: ein neuer Typ von Funktionsmaterialien. *Angew. Chem., Int. Ed.* **2010**, *122*, 4996−5016.

(6) Tan, C.; Zhang, H. Epitaxial growth of hetero-nanostructures based on ultrathin two-dimensional nanosheets. *J. Am. Chem. Soc.* **2015**, *137*, 12162−12174.

(7) Peng, X.; Schlamp, M. C.; Kadavanich, A. V.; Alivisatos, A. P. Epitaxial growth of highly luminescent CdSe/CdS core/shell nanocrystals with photostability and electronic accessibility. *J. Am. Chem. Soc.* **1997**, *119*, 7019−7029.

(8) Huang, Y.; Duan, X.; Wei, Q.; Lieber, C. M. Directed assembly of one-dimensional nanostructures into functional networks. *Science* **2001**, *291*, 630−633.

(9) Sun, X.; Guo, S.; Liu, Y.; Sun, S. Dumbbell-like PtPd-Fe3O4 nanoparticles for enhanced electrochemical detection of H2O2. *Nano Lett.* **2012**, *12*, 4859−4863.

(10) Costi, R.; Saunders, A. E.; Banin, U. Colloidal hybrid nanostructures: a new type of functional materials. *Angew. Chem., Int. Ed.* **2010**, *49*, 4878−4897.

(11) Figuerola, A.; Huis, M. v.; Zanella, M.; Genovese, A.; Marras, S.; Falqui, A.; Zandbergen, H. W.; Cingolani, R.; Manna, L. Epitaxial

DOI: 10.1021/acsami.7b15854
ACS Appl. Mater. Interfaces 2017, 9, 44550−44559

CdSe-Au nanocrystal heterostructures by thermal annealing. *Nano Lett.* **2010**, *10*, 3028−3036.
(12) Kang, J.; Li, J.; Li, S.-S.; Xia, J.-B.; Wang, L.-W. Electronic structural Moiré pattern effects on MoS2/MoSe2 2D heterostructures. *Nano Lett.* **2013**, *13*, 5485−5490.
(13) Ceballos, F.; Bellus, M. Z.; Chiu, H.-Y.; Zhao, H. Ultrafast charge separation and indirect exciton formation in a MoS2-MoSe2 van der Waals heterostructure. *ACS Nano* **2014**, *8*, 12717−12724.
(14) Li, M.-Y.; Shi, Y.; Cheng, C.-C.; Lu, L.-S.; Lin, Y.-C.; Tang, H.-L.; Tsai, M.-L.; Chu, C.-W.; Wei, K.-H.; He, J.-H.; et al. Epitaxial growth of a monolayer WSe2-MoS2 lateral pn junction with an atomically sharp interface. *Science* **2015**, *349*, 524−528.
(15) Gong, Y.; Lin, J.; Wang, X.; Shi, G.; Lei, S.; Lin, Z.; Zou, X.; Ye, G.; Vajtai, R.; Yakobson, B. I.; et al. Vertical and in-plane heterostructures from WS2/MoS2 monolayers. *Nat. Mater.* **2014**, *13*, 1135−1142.
(16) Huang, C.; Wu, S.; Sanchez, A. M.; Peters, J. J.; Beanland, R.; Ross, J. S.; Rivera, P.; Yao, W.; Cobden, D. H.; Xu, X. Lateral heterojunctions within monolayer MoSe2-WSe2 semiconductors. *Nat. Mater.* **2014**, *13*, 1096−1101.
(17) Gong, Y.; Lei, S.; Ye, G.; Li, B.; He, Y.; Keyshar, K.; Zhang, X.; Wang, Q.; Lou, J.; Liu, Z.; et al. Two-step growth of two-dimensional WSe2/MoSe2 heterostructures. *Nano Lett.* **2015**, *15*, 6135−6141.
(18) Yu, J. H.; Lee, H. R.; Hong, S. S.; Kong, D.; Lee, H.-W.; Wang, H.; Xiong, F.; Wang, S.; Cui, Y. Vertical heterostructure of two-dimensional MoS2 and WSe2 with vertically aligned layers. *Nano Lett.* **2015**, *15*, 1031−1035.
(19) Chen, K.; Wan, X.; Wen, J.; Xie, W.; Kang, Z.; Zeng, X.; Chen, H.; Xu, J.-B. Electronic properties of MoS2-WS2 heterostructures synthesized with two-step lateral epitaxial strategy. *ACS Nano* **2015**, *9*, 9868−9876.
(20) Tongay, S.; Fan, W.; Kang, J.; Park, J.; Koldemir, U.; Suh, J.; Narang, D. S.; Liu, K.; Ji, J.; Li, J.; et al. Tuning interlayer coupling in large-area heterostructures with CVD-grown MoS2 and WS2 monolayers. *Nano Lett.* **2014**, *14*, 3185−3190.
(21) Rigosi, A. F.; Hill, H. M.; Li, Y.; Chernikov, A.; Heinz, T. F. Probing interlayer interactions in transition metal dichalcogenide heterostructures by optical spectroscopy: MoS2/WS2 and MoSe2/WSe2. *Nano Lett.* **2015**, *15*, 5033−5038.
(22) Zhu, J.; Sakaushi, K.; Clavel, G.; Shalom, M.; Antonietti, M.; Fellinger, T.-P. A general salt-templating method to fabricate vertically aligned graphitic carbon nanosheets and their metal carbide hybrids for superior lithium ion batteries and water splitting. *J. Am. Chem. Soc* **2015**, *137*, 5480−5485.
(23) Miller, J. R.; Outlaw, R.; Holloway, B. Graphene double-layer capacitor with ac line-filtering performance. *Science* **2010**, *329*, 1637−1639.
(24) Bo, Z.; Zhu, W.; Ma, W.; Wen, Z.; Shuai, X.; Chen, J.; Yan, J.; Wang, Z.; Cen, K.; Feng, X. Vertically Oriented Graphene Bridging Active-Layer/Current-Collector Interface for Ultrahigh Rate Supercapacitors. *Adv. Mater.* **2013**, *25*, 5799−5806.
(25) Munshi, A. M.; Dheeraj, D. L.; Fauske, V. T.; Kim, D.-C.; van Helvoort, A. T.; Fimland, B.-O.; Weman, H. Vertically aligned GaAs nanowires on graphite and few-layer graphene: generic model and epitaxial growth. *Nano Lett.* **2012**, *12*, 4570−4576.
(26) Fan, X.; Zhou, H.; Guo, X. WC nanocrystals grown on vertically aligned carbon nanotubes: an efficient and stable electrocatalyst for hydrogen evolution reaction. *ACS Nano* **2015**, *9*, 5125−5134.
(27) Yang, J.; Wang, K.; Zhu, J.; Zhang, C.; Liu, T. Self-Templated Growth of Vertically Aligned 2H-1T MoS2 for Efficient Electrocatalytic Hydrogen Evolution. *ACS Appl. Mater. Interfaces* **2016**, *8*, 31702−31708.
(28) Tan, C.; Zhang, H. Two-dimensional transition metal dichalcogenide nanosheet-based composites. *Chem. Soc. Rev.* **2015**, *44*, 2713−2731.
(29) Duan, X.; Wang, C.; Shaw, J. C.; Cheng, R.; Chen, Y.; Li, H.; Wu, X.; Tang, Y.; Zhang, Q.; Pan, A.; et al. Lateral epitaxial growth of two-dimensional layered semiconductor heterojunctions. *Nat. Nanotechnol.* **2014**, *9*, 1024−1030.
(30) Mahjouri-Samani, M.; Lin, M.-W.; Wang, K.; Lupini, A. R.; Lee, J.; Basile, L.; Boulesbaa, A.; Rouleau, C. M.; Puretzky, A. A.; Ivanov, I. N. Patterned arrays of lateral heterojunctions within monolayer two-dimensional semiconductors. *Nat. Commun.* **2015**, *6*, No. 7749.
(31) Zhang, C.; Chen, Y.; Huang, J.-K.; Wu, X.; Li, L.-J.; Yao, W.; Tersoff, J.; Shih, C.-K. Visualizing band offsets and edge states in bilayer-monolayer transition metal dichalcogenides lateral heterojunction. *Nat. Commun.* **2016**, *7*, No. 10349.
(32) Lin, C.; Zhu, X.; Feng, J.; Wu, C.; Hu, S.; Peng, J.; Guo, Y.; Peng, L.; Zhao, J.; Huang, J.; et al. Hydrogen-incorporated TiS2 ultrathin nanosheets with ultrahigh conductivity for stamp-transferrable electrodes. *J. Am. Chem. Soc.* **2013**, *135*, 5144−5151.
(33) Chen, J. S.; Guan, C.; Gui, Y.; Blackwood, D. J. Rational Design of Self-Supported Ni3S2 Nanosheets Array for Advanced Asymmetric Supercapacitor with a Superior Energy Density. *ACS Appl. Mater. Interfaces* **2017**, *9*, 496−504.
(34) Chhowalla, M.; Shin, H. S.; Eda, G.; Li, L.-J.; Loh, K. P.; Zhang, H. The chemistry of two-dimensional layered transition metal dichalcogenide nanosheets. *Nat. Chem.* **2013**, *5*, 263−275.
(35) Pumera, M.; Sofer, Z.; Ambrosi, A. Layered transition metal dichalcogenides for electrochemical energy generation and storage. *J. Mater. Chem. A* **2014**, *2*, 8981−8987.
(36) Chhowalla, M.; Liu, Z.; Zhang, H. Two-dimensional transition metal dichalcogenide (TMD) nanosheets. *Chem. Soc. Rev.* **2015**, *44*, 2584−2586.
(37) Coleman, J. N.; Lotya, M.; O'Neill, A.; Bergin, S. D.; King, P. J.; Khan, U.; Young, K.; Gaucher, A.; De, S.; Smith, R. J.; et al. Two-dimensional nanosheets produced by liquid exfoliation of layered materials. *Science* **2011**, *331*, 568−571.
(38) Ramakrishna Matte, H.; Gomathi, A.; Manna, A. K.; Late, D. J.; Datta, R.; Pati, S. K.; Rao, C. MoS2 and WS2 analogues of graphene. *Angew. Chem., Int. Ed.* **2010**, *49*, 4059−4062.
(39) Yao, Y.; Lin, Z.; Li, Z.; Song, X.; Moon, K.-S.; Wong, C.-P. Large-scale production of two-dimensional nanosheets. *J. Mater. Chem.* **2012**, *22*, 13494−13499.
(40) Tan, C.; Zeng, Z.; Huang, X.; Rui, X.; Wu, X. J.; Li, B.; Luo, Z.; Chen, J.; Chen, B.; Yan, Q.; et al. Liquid-Phase Epitaxial Growth of Two-Dimensional Semiconductor Hetero-nanostructures. *Angew. Chem., Int. Ed.* **2015**, *54*, 1841−1845.
(41) Zeng, Z.; Yin, Z.; Huang, X.; Li, H.; He, Q.; Lu, G.; Boey, F.; Zhang, H. Single-Layer Semiconducting Nanosheets: High-yield preparation and device fabrication. *Angew. Chem., Int. Ed.* **2011**, *50*, 11093−11097.
(42) Wang, H.; Lu, Z.; Xu, S.; Kong, D.; Cha, J. J.; Zheng, G.; Hsu, P.-C.; Yan, K.; Bradshaw, D.; Prinz, F. B.; et al. Electrochemical tuning of vertically aligned MoS2 nanofilms and its application in improving hydrogen evolution reaction. *Proc. Natl. Acad. Sci. U.S.A.* **2013**, *110*, 19701−19706.
(43) Wang, S.; Wang, X.; Warner, J. H. All chemical vapor deposition growth of MoS2: h-BN vertical van der Waals heterostructures. *ACS Nano* **2015**, *9*, 5246−5254.
(44) Cheng, R.; Li, D.; Zhou, H.; Wang, C.; Yin, A.; Jiang, S.; Liu, Y.; Chen, Y.; Huang, Y.; Duan, X. Electroluminescence and photocurrent generation from atomically sharp WSe2/MoS2 heterojunction p-n diodes. *Nano Lett.* **2014**, *14*, 5590−5597.
(45) Zhou, X.; Liu, Y.; Ju, H.; Pan, B.; Zhu, J.; Ding, T.; Wang, C.; Yang, Q. Design and epitaxial growth of MoSe2-NiSe vertical heteronanostructures with electronic modulation for enhanced hydrogen evolution reaction. *Chem. Mater.* **2016**, *28*, 1838−1846.
(46) Wang, Z. Y.; Wang, Z. C.; Liu, W. T.; Xiao, W.; Lou, X. W. Amorphous CoSnO3@C nanoboxes with superior lithium storage capability. *Energy Environ. Sci.* **2013**, *6*, 87−91.
(47) Voiry, D.; Yang, J.; Chhowalla, M. Recent strategies for improving the catalytic activity of 2D TMD nanosheets toward the hydrogen evolution reaction. *Adv. Mater.* **2016**, *28*, 6197−6206.
(48) Zheng, Y.-R.; Gao, M.-R.; Yu, Z.-Y.; Gao, Q.; Gao, H.-L.; Yu, S.-H. Cobalt diselenide nanobelts grafted on carbon fiber felt: an efficient and robust 3D cathode for hydrogen production. *Chem. Sci.* **2015**, *6*, 4594−4598.

DOI: 10.1021/acsami.7b15854
ACS Appl. Mater. Interfaces 2017, 9, 44550−44559

(49) Deng, S.; Zhong, Y.; Zeng, Y.; Wang, Y.; Yao, Z.; Yang, F.; Lin, S.; Wang, X.; Lu, X.; Xia, X.; Tu, J. Directional Construction of Vertical Nitrogen-Doped 1T-2H MoSe2/Graphene Shell/Core Nanoflake Arrays for Efficient Hydrogen Evolution Reaction. *Adv. Mater.* **2017**, *29*, No. 1700748.
(50) Xie, J.; Zhang, J.; Li, S.; Grote, F.; Zhang, X.; Zhang, H.; Wang, R.; Lei, Y.; Pan, B.; Xie, Y. Controllable disorder engineering in oxygen-incorporated MoS2 ultrathin nanosheets for efficient hydrogen evolution. *J. Am. Chem. Soc.* **2013**, *135*, 17881−17888.
(51) Ma, L.; Zhou, X.; Xu, L.; Xu, X.; Zhang, L.; Chen, W. Ultrathin few-layered molybdenum selenide/graphene hybrid with superior electrochemical Li-storage performance. *J. Power Sources* **2015**, *285*, 274−280.
(52) Shi, Y.; Hua, C.; Li, B.; Fang, X.; Yao, C.; Zhang, Y.; Hu, Y. S.; Wang, Z.; Chen, L.; Zhao, D.; et al. Highly Ordered Mesoporous Crystalline MoSe2 Material with Efficient Visible-Light-Driven Photocatalytic Activity and Enhanced Lithium Storage Performance. *Adv. Funct. Mater.* **2013**, *23*, 1832−1838.
(53) Wang, M.; Li, G.; Xu, H.; Qian, Y.; Yang, J. Enhanced lithium storage performances of hierarchical hollow MoS_2 nanoparticles assembled from nanosheets. *ACS Appl. Mater. Interfaces* **2013**, *5*, 1003−1008.
(54) Xiao, J.; Choi, D.; Cosimbescu, L.; Koech, P.; Liu, J.; Lemmon, J. P. Exfoliated MoS2 nanocomposite as an anode material for lithium ion batteries. *Chem. Mater.* **2010**, *22*, 4522−4524.
(55) Wang, Z.; Luan, D.; Madhavi, S.; Hu, Y.; Lou, X. W. D. Assembling carbon-coated α-Fe2O3 hollow nanohorns on the CNT backbone for superior lithium storage capability. *Energy Environ. Sci.* **2012**, *5*, 5252−5256.
(56) Wang, X.; Fan, Y.; Susantyoko, R. A.; Xiao, Q.; Sun, L.; He, D.; Zhang, Q. High areal capacity Li ion battery anode based on thick mesoporous Co3O4 nanosheet networks. *Nano Energy* **2014**, *5*, 91−96.
(57) Liu, B.; Zhang, J.; Wang, X.; Chen, G.; Chen, D.; Zhou, C.; Shen, G. Hierarchical three-dimensional ZnCo2O4 nanowire arrays/carbon cloth anodes for a novel class of high-performance flexible lithium-ion batteries. *Nano Lett.* **2012**, *12*, 3005−3011.
(58) Yu, L.; Wang, Z.; Zhang, L.; Wu, H. B.; Lou, X. W. D. TiO2 nanotube arrays grafted with Fe2O3 hollow nanorods as integrated electrodes for lithium-ion batteries. *J. Mater. Chem. A* **2013**, *1*, 122−127.
(59) Laruelle, S.; Grugeon, S.; Poizot, P.; Dolle, M.; Dupont, L.; Tarascon, J. On the origin of the extra electrochemical capacity displayed by MO/Li cells at low potential. *J. Electrochem. Soc.* **2002**, *149*, A627−A634.
(60) Poizot, P.; Laruelle, S.; Grugeon, S.; Dupont, L.; Tarascon, J. Nano-sized transition-metal oxides as negative-electrode materials for lithium-ion batteries. *Nature* **2000**, *407*, 496−499.
(61) Zhang, W. M.; Wu, X. L.; Hu, J. S.; Guo, Y. G.; Wan, L. J. Carbon Coated Fe3O4 Nanospindles as a Superior Anode Material for Lithium-Ion Batteries. *Adv. Funct. Mater.* **2008**, *18*, 3941−3946.
(62) Lou, X. W.; Li, C. M.; Archer, L. A. Designed synthesis of coaxial SnO2@ carbon hollow nanospheres for highly reversible lithium storage. *Adv. Mater.* **2009**, *21*, 2536−2539.
(63) Jia, L.; Sun, X.; Jiang, Y.; Yu, S.; Wang, C. A Novel MoSe2-Reduced Graphene Oxide/Polyimide Composite Film for Applications in Electrocatalysis and Photoelectrocatalysis Hydrogen Evolution. *Adv. Funct. Mater.* **2015**, *25*, 1814−1820.

DOI: 10.1021/acsami.7b15854
ACS Appl. Mater. Interfaces 2017, 9, 44550−44559